Applied Physics Letters

Resemblance between motile and magnetically actuated sperm cells

Cite as: Appl. Phys. Lett. **116**, 063702 (2020); https://doi.org/10.1063/1.5142470
Submitted: 13 December 2019 . Accepted: 28 January 2020 . Published Online: 10 February 2020

Islam S. M. Khalil, Veronika Magdanz, Juliane Simmchen, Anke Klingner, and Sarthak Misra

Applied Physics Letters ARTICLE scitation.org/journal/apl

Resemblance between motile and magnetically actuated sperm cells

Cite as: Appl. Phys. Lett. **116**, 063702 (2020); doi: 10.1063/1.5142470
Submitted: 13 December 2019 · Accepted: 28 January 2020 ·
Published Online: 10 February 2020

Islam S. M. Khalil,[1,a)] Veronika Magdanz,[2,a)] Juliane Simmchen,[3] Anke Klingner,[4] and Sarthak Misra[1,5]

AFFILIATIONS

[1]Department of Biomechanical Engineering, University of Twente, Enschede 7522 NB, The Netherlands
[2]Applied Zoology, Faculty of Biology, Technical University of Dresden, Dresden 01062, Germany
[3]Physical Chemistry, Technical University of Dresden, Dresden 01062, Germany
[4]Department of Physics, the German University in Cairo, Cairo 11835, Egypt
[5]Department of Biomedical Engineering, University of Groningen and University Medical Center Groningen, Groningen 9713 AV, The Netherlands

[a)]**Authors to whom correspondence should be addressed:** i.s.m.khalil@utwente.nl and veronika.magdanz@tu-dresden.de

ABSTRACT

The active flagellum propels a motile sperm cell by traveling bending waves. Here, we demonstrate that non-motile cells have the capacity to be wirelessly actuated by external magnetic fields and reveal insights into their propulsion characteristics. Partial coating of the sperm head with nanoparticle aggregates is achieved by electrostatic-based self-assembly. The coating enables propagation of helical traveling waves along the passive flagellum under the action of a periodic magnetic field. We compare the waveforms of active and passive flagellated motion and show noticeable asymmetry in the case of magnetically actuated cells, leading to lower linearity (LIN = VSL/VCL) of the taken pathway. The average curvature of the flagellar beat cycle is $10.4 \pm 8.1\,\text{rad mm}^{-1}$ (mean ± s.d.) for an active flagellum, whereas the curvature of a passive flagellum exhibits a linear increase ($37.4 \pm 18.1\,\text{rad mm}^{-1}$) and decreases toward the distal end. We also show that the maximum amplitude of the bending wave occurs at the distal end of the active flagellum and at the middle of the passive flagellum. Our experiments also show the ability of the actuating field to control the rate of progression of the bending waves along the passive flagellum to match that of motile cells.

The development of microrobots able to be wirelessly controlled has gone through two distinct methods of implementation: geometric downscaling[1–3] and the utilization of biological motors.[4–6] As the size of these devices approaches the microscale, in the case of downscaling, it is apparent that several hurdles have to be overcome. For example, the integration of power sources and the propulsion mechanism is limited by downscaling. Geometric scaling has been enabled through the wirelessly transmitted power to these devices by magnetic,[7–10] acoustic,[11] light,[12] and chemical[13,14] sources. Regardless of the power source, it has to be transduced into motion to propel rigid or flexible structures mostly in the shape of a helix[15] or straight wire.[16] In either case, a propulsive force is generated by a corkscrew motion or a traveling wave to generate propulsion in low Reynolds (*Re*) numbers.[17] The second method is implemented by using a motile or non-motile micro-organism or cell, either to provide propulsion[18] or as a template.[19]

This Letter studies the motion characteristics of motile and magnetically actuated non-motile bovine sperm cells and reveals insights into the differences between their natural and artificial rotary motors (Table I). Spermatozoa have recently been suggested as components of microrobots due to their strong flagellar driving source and ability to take up drugs,[20,21] Furthermore, spermatozoa navigate through the female reproductive tract regardless of fluid flow, chemicals, temperature, and near-surface effects,[22–24] and most existing sperm micromotors depend on the propulsive force of the active flagellum and are sensitive to physiological conditions (pH, temperature, and chemicals).[25] In this Letter, we present the properties of magnetically actuated passive flagella of dead sperm cells. The swimming efficacy of the magnetically actuated cells is insensitive to these physiological conditions and lower than that of live cells, which is expected owing to the difference in the actuation mechanism. However, the actuation of passive flagella reveals insights into the desirable flagellar waveforms to design efficient microswimmers.

Spermatozoa perform their bending motion by switching molecular motors (dyneins) between a compression and distension state between the microtubule, which are situated along the flagellum.[26] The dynein motors are driven by adenosine triphosphate (ATP) as the

TABLE I. Motile and magnetically actuated sperm cells are fluorescently labeled with green SYBR14 and red propidium iodide stains to indicate live and dead cells. The flagellum is 60 μm, and the head width and length are 4.5 μm and 10 μm. The scale bar is 5 μm.

	Motile sperm cell	Magnetic sperm cell
Image		
Composition	Live bull sperm cell	Dead bull sperm cell + nanoparticles
Actuation	ATP-driven dynein motors (active flagellum)	Magnetic torque on the head (passive flagellum)
Power	Energy metabolism of the cell	Magnetic energy from the external source

energy source, which is provided by the energy metabolism of the sperm cell. Sperm motion is typically analyzed using four parameters:[27] (1) curvilinear velocity (VCL), which describes the actual sperm path; (2) average path velocity (VAP); (3) straight line velocity (VSL); and (4) linearity (LIN = VSL/VCL), which is a measure of the straightness of the path.

In order to experimentally compare the swimming characteristics of motile and magnetically actuated cells, two-dimensional projections of the motion of each cell are analyzed. Non-motile cells are coated with rice grain-shaped nanoparticles at the head of the cell. A solution of $FeCl_3 \cdot H_2O$ is aged with NaH_2PO_4 for 72 h at 100 °C, resulting in positively charged elongated 100 nm iron oxide nanoparticles that adhere to the negatively charged bovine sperm cells.[28] The magnetic moment per cell is measured using a vibrating sample magnetometer as, $m = 1.5 \times 10^{-11}$ A m^2 at a magnetic field of 2 mT. Sperm cells are recorded during regular beating in modified tyrode's albumine lactate pyruvate medium, and the detailed shape of their active flagella is measured to quantitatively compare their waveform with magnetically actuated passive flagella. Video recording is done with a frame rate of 500 frames per second and 640× total magnification and phase contrast. The shape of the flagellum is characterized by the tangent angle $[\varphi(s,t)]$ enclosed between the long axis $[\mathbf{e}_1(t)]$ of the head and the local tangent along the arc length s (Fig. 1, Multimedia view). Figure 1(a) shows a cell over half beat cycle, whereas Fig. 1(b) shows a magnetically actuated sperm cell in water with viscosity ($\eta = 1$ mPa s). The actuation is achieved by applying a uniform time-dependent magnetic field and exerting magnetic torque (no magnetic force is applied) on the dipole of the cell using a tri-axial Helmholtz coil system. The cells are actuated with the magnetic field ($B = 2$ mT), leading to magnetic torque on the order of 3×10^{-14} N m. The field continuously rotates in the yz-plane about the x-axis, and the head executes a circular orbit leading to propagation of transverse waves along the passive flagellum.

In the case of motile cells [Fig. 1(a)], bending waves along the active flagellum are generated and governed by the balance between the elastic and drag forces in low-*Re* ($\sim 10^{-4}$). The inertial forces are negligible,[17] and the relation between the viscous force and the velocity of a segment is linear over the beat cycle of the flagellum.[29,30] Qualitatively similar bending waves are also generated along the passive flagellum of magnetically actuated cells under the action of an oscillating field with the exception that they originate from magnetic torque exerted on the

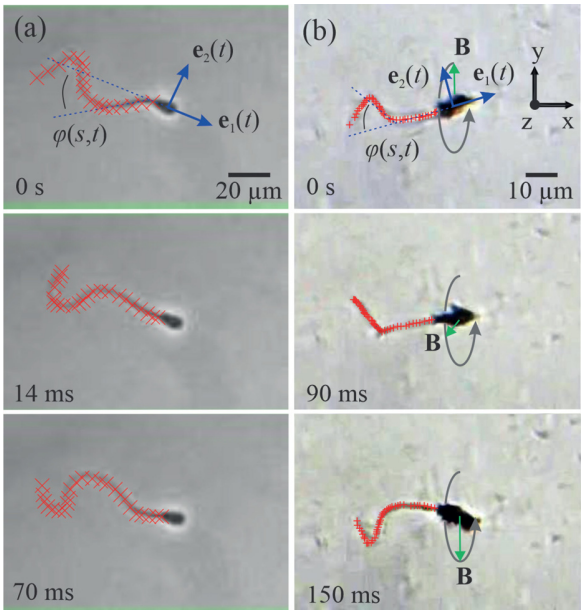

FIG. 1. Motile and magnetically actuated sperm cells swim by traveling waves (over half beat cycle). (a) Sperm cell swims by energy metabolism ($f = 7.7$ Hz). (b) Magnetically actuated cell swims by rotating magnetic fields ($f = 6$ Hz) about the x-axis. The field (green arrow) rotates in the yz-plane, and magnetic torque is converted into propulsion. The circular gray arrow indicates the direction of rotation. The red markers indicate the tail deformation used to measure the tangent angle $[\phi(s,t)]$. Multimedia views: https://doi.org/10.1063/1.5142470.1; https://doi.org/10.1063/1.5142470.2

head. Therefore, the magnetically actuated sperm cells are governed by the balance between the magneto-elastic and drag forces as

$$\kappa \frac{\partial^4 \varphi}{\partial s^4}(s,t) + \xi_\perp \frac{\partial \varphi}{\partial t}(s,t) = 0. \tag{1}$$

The first term in Eq. (1) characterizes the coupling between the flagellum with bending stiffness (κ) and magnetic torque, whereas the second term describes the hydrodynamic coupling in low-*Re*, where $\xi_\perp$ is the perpendicular drag coefficient and is considered constant owing to the low-*Re* characteristics.[29,30] The flagellum is rigidly anchored to the head with an average magnetic moment m, and the magnetic torque is specified through $\varphi(0,t) = 0$ and $\partial\varphi/\partial s(0,t) = mB \sin \omega t$. The second condition implies that the local curvature of the flagellum is controlled by the external magnetic torque and controls the propagation of harmonic waves along the flagellum. The tangent angle of the flagellum can be decomposed by the zeroth and first Fourier coefficients as follows:[31]

$$\varphi(s,t) \approx \phi(s) + \psi(s)e^{i\omega t} + \psi^*(s)e^{-i\omega t}, \tag{2}$$

where $\phi(s)$ is the zeroth mode and characterizes the time-averaged mean shape of the flagellum. Furthermore, $\psi(s)$ and $\psi^*(s)$ are the first mode and its complex conjugate, and its magnitude characterizes the bending amplitude along the flagellum. Equation (1) gives the following relation between the hydrodynamic and magneto-elastic coupling:

$$-\frac{i}{\ell_\omega^4}(\psi e^{i\omega t} - \psi^* e^{-i\omega t}) = \frac{\partial^4 \phi}{\partial s^4} + \frac{\partial^4 \psi}{\partial s^4} e^{i\omega t} + \frac{\partial^4 \psi^*}{\partial s^4} e^{-i\omega t}, \tag{3}$$

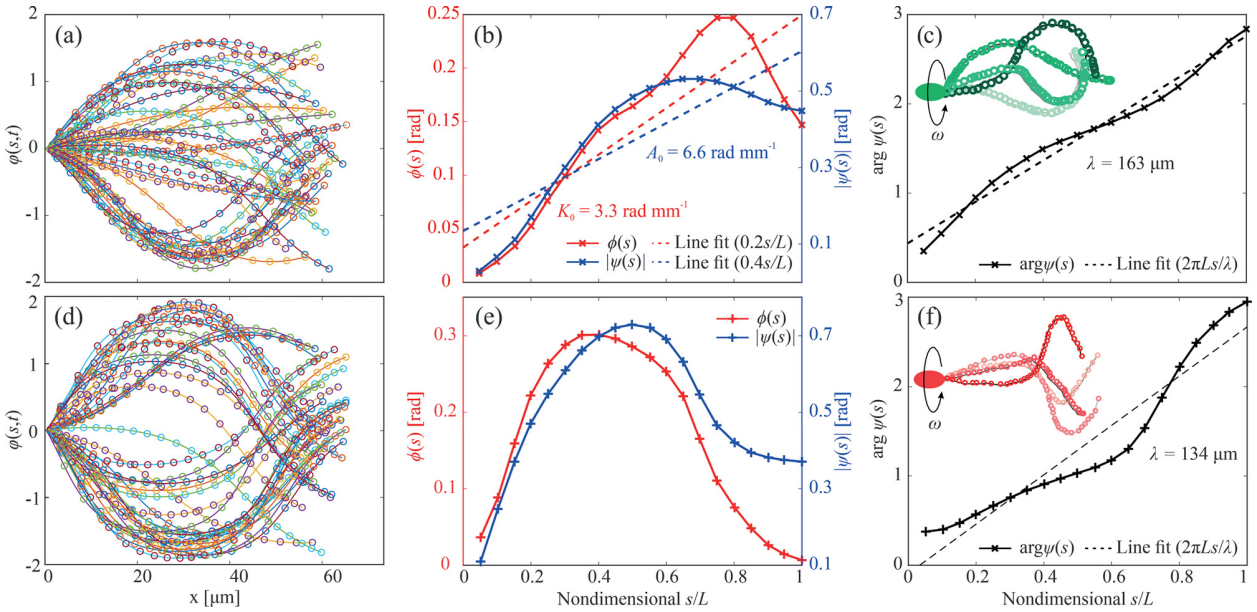

FIG. 2. Flagellar waveforms of motile and magnetically actuated sperm cells are characterized. (a) The tangent angle ($\varphi(s,t)$) is determined from the flagellar deformation across a complete beat cycle. (b) The mean flagellar curvature is 3.3 rad mm^{-1}, whereas the amplitude rise is 6.6 rad mm^{-1}. (c) $\lambda = 163$ μm. (d) The tangent angle of a magnetically actuated sperm cell. (e) The curvature increases and decreases along the flagellum, while the maximum amplitude occurs at 0.5L from the proximal end of the cell. (f) $\lambda = 134$ μm. The insets show the measured waveforms over half beat cycle. Darker curves indicate later times.

where $\ell_\omega = (\kappa/\omega\xi_\perp)^{1/4}$ is the characteristic penetration length.[32] The hydrodynamics can be simplified by using the ideal flagellar waveform. Riedel-Kruse *et al.* have shown that the ideal flagellar waveform consists of an arc with a constant curvature [$\phi(s) = K_0 s$] and a bending amplitude that increases along the flagellum linearly ($\psi(s) = A_0 s$), where K_0 and A_0 are the curvature and the bending amplitude of the flagellum, respectively.[31] Under these conditions, we have $\partial^4\phi/\partial s^4 = 0$, $\partial^4\psi/\partial s^4 = 0$, and $\partial^4\psi^*/\partial s^4 = 0$. In addition, since the characteristic penetration length is nonzero for nonzero actuation frequency $\omega = 2\pi f$, we obtain

$$\mathrm{Re}\{\psi(s)\}\sin\omega t + \mathrm{Im}\{\psi(s)\}\cos\omega t = 0. \quad (4)$$

Equation (4) defines the phase angle, $\Phi = -\arg\psi(s)$, which characterizes the progression of the wave along the flagellum. The tangent angle is determined using the measured flagellum deformation [Fig. 2(a)], and the zeroth and first Fourier modes are calculated using Eq. (2). The zeroth coefficient $\phi(s)$ for an active flagellum is used to determine K_0 by fitting a line to the data, as shown in Fig. 2(b). Similar to the curvature, A_0 is determined by fitting a line to $|\psi(s)|$. Therefore, K_0 and A_0 of the motile cell in this trial are 3.3 rad mm^{-1} and 6.6 rad mm^{-1}, respectively, and the curvature and bending moment are approximately linear with the exception of the proximal and distal ends. Figure 2(c) shows the measured phase angle. The wavelength (λ) is determined to be 163 μm by fitting a line $2\pi Ls/\lambda$ to the phase angle, where L is the length of the flagellum. This experiment is implemented using ten different sperm cells for three consecutive periods of motion, and average K_0, A_0, and λ are provided in Table II. We repeat the same test for magnetically actuated sperm cells [Fig. 2(d)]. Unlike the active flagellum, the curvature of the passive flagellum increases and then decreases toward the distal end, while the maximum amplitude of the bending wave occurs at 0.5L from the proximal end [Fig. 2(e)]. Therefore, the curvature and bending moment are calculated for, $0 < s < 0.5L$, to be 37.4 ± 18.1 rad mm^{-1} and 15.9 ± 7.0 rad mm^{-1}, respectively. The rotation of the magnetic head also induces wave propagation with an average wavelength, $\lambda = 150 \pm 13$ μm [Fig. 2(f)].

Figure 2(b) shows that the curvature increases linearly, except for the proximal and distal ends of the active flagellum, whereas Fig. 2(e) shows that the curvature increases and then decreases toward the distal end of the passive flagellum. We attribute this behavior to the difference in actuation, as the active flagellum has distributed actuation, whereas the passive flagellum is actuated by the exerted magnetic moment at the head only. Furthermore, the passive bending stiffness of live spermatozoa depends on the amount of ATP present in the medium.[26,34] In the case of magnetically actuated sperm cells, the bending stiffness of the flagellum cannot be estimated because the cells

TABLE II. Characterized waveform and motion variables.

Sperm cell	Motile cell	Magnetic cell
K_0 (rad mm^{-1})	10.4 ± 8.1	37.4 ± 18.1 ($s \in 0 : 0.5L$)
A_0 (rad mm^{-1})	6.7 ± 2.2	15.9 ± 7 ($s \in 0 : 0.5L$)
λ (μm)	198 ± 44	150 ± 13
VSL (μm s^{-1})	101.6 ± 31.6	6.3 ± 1.2
VCL (μm s^{-1})	225.4 ± 77.1	24.9 ± 14.4
LIN (VSL/VCL)	0.48 ± 0.18	0.28 ± 0.1
VAP (μm s^{-1})	113.2 ± 31.7	7.3 ± 1.1

are not alive anymore and the state of interaction has not yet been quantified for non-metabolizing sperm cells. Therefore, the difference in the flagellar waveform can be attributed to differences between internal and external power generation. Similar to the curvature, the bending moment along the flagellum is mostly linear in the case of the motile cells, while the magnetically actuated cells show a decreasing amplitude along the flagellum. The curvature and bending moment also reveal that the asymmetry of the flagellar mean shape is more evident in the case of magnetically actuated cells. In contrast to the curvature and bending amplitude, the rate of propagation of the elastic wave of the motile and magnetic cells is quite similar [Figs. 2(c) and 2(f)]. The average slope of the phase angle for the motile cells is $2\pi/\lambda = 2\pi/185$, whereas magnetically actuated cells have an average slope of $2\pi/134$, at an actuation frequency of 6 Hz. Therefore, the magnetic field enables non-motile cells to rotate with respect to $\mathbf{e}_1$ while displaying helical flagellar waves like motile cells.

The wave variables dictate the time-dependent deformation of the flagellum. Therefore, the force exerted by the flagellum is determined using the resistive-force theory (RFT)[29,33] for a range of wave variables (Table II). Figure 3 shows the influence of A_0 and λ on the swimming velocity. The green and red shaded regions indicate the minimum and maximum $F/(\eta\omega A_{\max}^2)$ for motile and magnetic cells, respectively. Equation (2) is integrated to determine the deformation of the flagellum $(y(x,t))$ in the material frame of the cell $(\mathbf{e}_1, \mathbf{e}_2)$. The deformation is used to determine the following force using RFT for the tangential $(\xi_\perp)$ and perpendicular $(\xi_{||})$ drag coefficients in the study by Gray and Hancock[29] and Lighthill:[33]

$$F = \int_0^\lambda \left(\frac{(\xi_\perp - \xi_{||})\frac{\partial y}{\partial t}\frac{\partial y}{\partial x} - f\lambda\left(\xi_{||} + \xi_\perp\left(\frac{\partial^2 y}{\partial x^2}\right)^2\right)}{1 + \left(\frac{\partial^2 y}{\partial x^2}\right)^2} \right) dx. \quad (5)$$

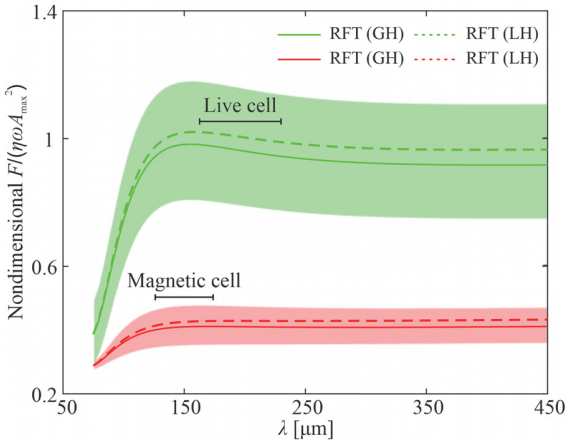

FIG. 3. The thrust force (F) is calculated using (5) based on the average (K_0) and (A_0) for a range of wavelengths (λ). The solid and dashed lines indicate average forces calculated by the resistive-force theory (RFT) in the studies by Gray and Hancock[29] and Lighthill (LH),[33] respectively. η, ω, and A_{max} are the viscosity, angular frequency, and the maximum amplitude, respectively. Minimum and maximum $F/(\eta\omega A_{max}^2)$ are calculated using RFT in the study by Gray and Hancock and indicated using the shaded regions.

We observe that the wave variables of motile cells generate greater force than magnetically actuated cells. The cells display a flagellar wave accompanied by a rotation of the body with respect to the long axis of the head ($\mathbf{e}_1$), and swim along a curved path. This motion is characterized by an average VSL of $101.6 \pm 31.6\ \mu m\ s^{-1}$ and a VCL of $225.4 \pm 77.1\ \mu m\ s^{-1}$, as shown in Fig. 4 (Multimedia view). A drastic decrease in the swimming speed is observed in the case of magnetically actuated cells, with an average VSL of $6.3 \pm 1.2\ \mu m\ s^{-1}$ and a VCL of $24.9 \pm 14.4\ \mu m\ s^{-1}$. This decrease is attributed partially to the additional drag exerted on the nanoparticle aggregates that coat the sperm head. The swimming velocity of the cell is dictated by the asymptotic force balance between the thrust force generated by the tail and the drag force on the head. Regardless of the difference in swimming speed, which is attributed to the calculated thrust force (Fig. 3), the average LIN indicates another fundamental difference in flagellar propulsion. The average linearity is 0.48 ± 0.18 and 0.28 ± 0.1 for motile and magnetically actuated sperm cells, respectively. The curvature of the paths taken by magnetically actuated sperm cells is larger than that of motile cells. Figures 2(b) and 2(e) show the asymmetry of the mean shape. This asymmetry is noticeable in the case of magnetically actuated cells, leading to a greater deviation between VSL and VCL. The insets in Figs. 2(c) and 2(f) show the flagellar waveform. These waveforms indicate qualitatively that the asymmetry is more noticeable for magnetically actuated sperm cells, leading to lower LIN.

In this Letter, we show the influence of distributed bending and localized external actuation of motile and non-motile cells, respectively. Waveform analysis reveals that maximum amplitude of the bending wave occurs at $0.75L$ and $0.5L$ from the proximal end of the

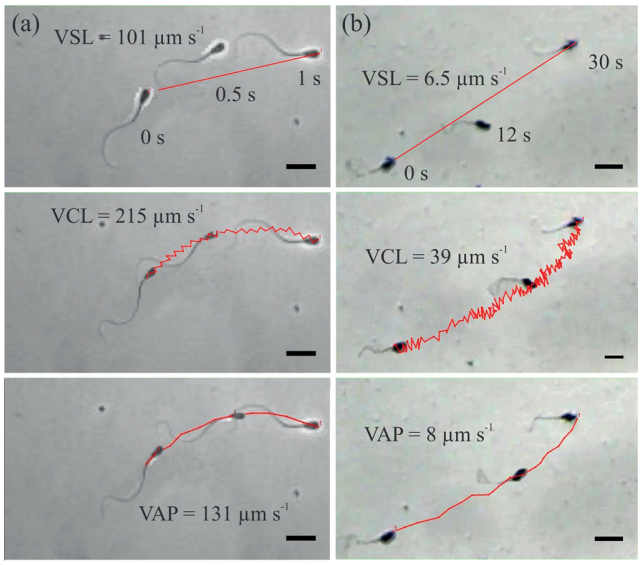

FIG. 4. Trajectories of motile and magnetically actuated sperm cells. (a) Straight line velocity (VSL), curvilinear velocity (VCL), and average path velocity (VAP) for motile bull sperm. (b) VSL, VCL, and VAP are calculated from magnetically actuated sperm cells. Scale bars are 20 μm. Multimedia views: https://doi.org/10.1063/1.5142470.3; https://doi.org/10.1063/1.5142470.4; https://doi.org/10.1063/1.5142470.5; https://doi.org/10.1063/1.5142470.6; https://doi.org/10.1063/1.5142470.7; https://doi.org/10.1063/1.5142470.8

active and passive flagellum, respectively, leading to greater swimming speed of the motile cells. Therefore, the actuation of the passive flagellum at the proximal end does not resemble the distributed actuation of the flagellum. However, the incorporation of nanoparticles opens up additional possibilities to resemble waveform patterns of motile cells, such as the use of different nanoparticles that will selectively adhere to certain locations along the flagellum, enabling non-uniform distributed actuation. In conclusion, this work contributes to the understanding of how motile sperm cells perform their efficient motion in low-*Re*. The actuation of a passive flagellum enables us to understand how to design efficient microswimmers. It would be essential to dope the non-motile cells with different magnetic entities on different locations. Furthermore, a combination of attractive and repulsive particles might enlarge the amplitude of the flagellar wave toward the distal end and enhance the propulsion. This would also mimic the interactions of molecular motors of sperm cells.

This work was supported in part by the European Research Council (ERC) through the European Union's Horizon 2020 Research and Innovation Program under Grant No. 638428 (Project ROBOTAR). This work was also supported by the Zukunftskonzept of the TU Dresden, funded by the excellence initiative of the German Research Foundation (DFG) and the Volkswagen foundation, Grant No. nr91619.

REFERENCES

[1]L. Zhang, J. J. Abbott, L. Dong, B. E. Kratochvil, D. Bell, and B. J. Nelson, Appl. Phys. Lett. **94**, 064107 (2009).
[2]K. E. Peyer, L. Zhang, and B. J. Nelson, Nanoscale **5**, 1259–1272 (2013).
[3]A. Ghosh and P. Fischer, Nano Lett. **9**, 2243–2245 (2009).
[4]B. Behkam and M. Sitti, Appl. Phys. Lett. **90**, 023902 (2007).
[5]V. Magdanz, S. Sanchez, and O. G. Schmidt, Adv. Mater. **25**, 6581–6588 (2013).
[6]B. J. Williams, S. V. Anand, J. Rajagopalan, and M. T. A. Saif, Nat. Commun. **5**, 3081 (2014).
[7]R. Dreyfus, J. Baudry, M. L. Roper, M. Fermigier, H. A. Stone, and J. Bibette, Nature **437**, 862–865 (2005).
[8]M. P. Kummer, J. J. Abbott, B. E. Kartochvil, R. Borer, A. Sengul, and B. J. Nelson, IEEE Trans. Rob. **26**, 1006–1017 (2010).
[9]O. S. Pak, W. Gao, J. Wang, and E. Lauga, Soft Matter **7**, 8169–8181 (2011).
[10]G. Adam, S. Chowdhury, M. Guix, B. Johnson, C. Bi, and D. Cappelleri, Robotics **8**, 69 (2019).
[11]J. Li, T. Li, T. Xu, M. Kiristi, W. Liu, Z. Wu, and J. Wang, Nano Lett. **15**, 4814–4821 (2015).
[12]S. Palagi, A. G. Mark, S. Y. Reigh, K. Melde, T. Qiu, H. Zeng, C. Parmeggiani, D. Martella, A. Sanchez-Castillo, N. Kapernaum, F. Giesselmann, D. S. Wiersma, E. Lauga, and P. Fischer, Nat. Mater. **15**, 647–653 (2016).
[13]W. F. Paxton, K. C. Kistler, C. C. Olmeda, A. Sen, S. K. S. Angelo, Y. Cao, T. E. Mallouk, P. E. Lammert, and V. H. Crespi, J. Am. Chem. Soc. **12**, 13424–13431 (2004).
[14]S. Fournier-Bidoz, A. C. Arsenault, I. Manners, and G. A. Ozin, Chem. Commun. **2005**, 441–443.
[15]J. J. Abbott, K. E. Peyer, L. Dong, and B. Nelson, Int. J. Rob. Res. **28**, 1434–1447 (2009).
[16]I. S. M. Khalil, H. C. Dijkslag, L. Abelmann, and S. Misra, Appl. Phys. Lett. **104**, 223701 (2014).
[17]E. M. Purcell, Am. J. Phys. **45**, 3–11 (1977).
[18]R. W. Carlsen, M. R. Edwards, J. Zhuang, C. Pacoret, and M. Sitti, Lab Chip **14**, 3850–3859 (2014).
[19]X. Yan, Q. Zhou, M. Vincent, Y. Deng, J. Yu, J. Xu, T. Xu, T. Tang, L. Bian, Y.-X. J. Wang, K. Kostarelos, and L. Zhang, Sci. Rob. **2**, eaaq1155 (2017).
[20]V. Magdanz, M. Medina-Sánchez, L. Schwarz, H. Xu, J. Elgeti, and O. G. Schmidt, Adv. Mater. **29**, 1606301 (2017).
[21]H. Xu, M. Medina-Sanchez, V. Magdanz, L. Schwarz, F. Hebenstreit, and O. G. Schmidt, ACS Nano **12**, 327–337 (2018).
[22]J.-J. Chung, S.-H. Shim, R. A. Everley, S. P. Gygi, X. Zhuang, and D. E. Clapham, Cell **157**, 808–822 (2014).
[23]B. M. Friedrich and F. Julicher, Proc. Natl. Acad. Sci. U. S. A. **104**, 13256–13261 (2007).
[24]A. G. A. Bahat, I. Tur-Kaspa, L. C. Giojalas, H. Breitbart, and M. Eisenbach, Nat. Med. **9**, 149–150 (2003).
[25]C. Chen, X. Chang, P. Angsantikul, J. Li, B. E.-F. de Ávila, E. Karshalev, W. Liu, F. Mou, S. He, R. Castillo, J. G. Y. Liang, L. Zhang, and J. Wang, Adv. Biosyst. **2**, 1700160 (2018).
[26]C. B. Lindemann and K. A. Lesich, J. Cell Sci. **123**, 519–528 (2010).
[27]W. H. Organization, *WHO Laboratory Manual for the Examination and Processing of Human Semen*, 5th ed. (World Health Organization, Switzerland, 2010).
[28]V. Magdanz, J. Gebauer, P. S. abd, S. Eltoukhy, D. Voigt, and J. Simmchen, Adv. Biosyst. **3**, 1900061 (2019).
[29]J. Gray and G. J. Hancock, J. Exp. Biol. **32**, 802–814 (1955) available at https://jeb.biologists.org/content/32/4/802.
[30]K. E. Machin, J. Exp. Biol. **35**, 796–806 (1958) available at https://jeb.biologists.org/content/35/4/796.
[31]B. M. Friedrich, I. H. Riedel-Kruse, J. Howard, and F. Jülicher, J. Exp. Biol. **213**, 1226–1234 (2010).
[32]T. S. Yu, E. Lauga, and A. E. Hosoi, Phys. Fluids **18**, 091701 (2006).
[33]J. Lighthill, SIAM Rev. **18**, 161–230 (1976).
[34]K. A. Lesich, D. W. Pelle, and C. B. Lindemann, Biophys. J. **95**, 472–482 (2008).